AGU PUBLICATIONS

Geophysical Research Letters

RESEARCH LETTER
10.1002/2014GL062940

Key Points:
- Bright oscillating lines in SAR scenes over sea ice are caused by ocean waves
- Swell orbital velocities, hence height, are estimated from line oscillations
- Sentinel-1 wave mode can provide swell attenuation coefficients

Correspondence to:
F. Ardhuin,
ardhuin@ifremer.fr

Citation:
Ardhuin, F., F. Collard, B. Chapron, F. Girard-Ardhuin, G. Guitton, A. Mouche, and J. E. Stopa (2015), Estimates of ocean wave heights and attenuation in sea ice using the SAR wave mode on Sentinel-1A, *Geophys. Res. Lett.*, *42*, 2317–2325, doi:10.1002/2014GL062940.

Received 19 DEC 2014
Accepted 26 FEB 2015
Accepted article online 3 MAR 2015
Published online 1 APR 2015

Estimates of ocean wave heights and attenuation in sea ice using the SAR wave mode on Sentinel-1A

Fabrice Ardhuin[1,2], Fabrice Collard[3], Bertrand Chapron[1], Fanny Girard-Ardhuin[1], Gilles Guitton[3], Alexis Mouche[1], and Justin E. Stopa[1]

[1]Ifremer, Laboratoire d'Océanographie Spatiale, Brest, France, [2]Laboratoire de Physique des Océans, UMR 6523, CNRS-Ifremer-UBO-IRD, Brest, France, [3]OceanDataLab, Plouzan'e, France

Abstract Swell evolution from the open ocean into sea ice is poorly understood, in particular the amplitude attenuation expected from scattering and dissipation. New synthetic aperture radar (SAR) data from Sentinel-1A wave mode reveal intriguing patterns of bright oscillating lines shaped like instant noodles. We investigate cases in which the oscillations are in the azimuth direction, around a straight line in the range direction. This observation is interpreted as the distortion by the SAR processing of crests from a first swell, due to the presence of a second swell. Since deviations from a straight line should be proportional to the orbital velocity toward the satellite, swell height can be estimated, from 1.5 to 5 m in the present case. The evolution of this 13 s period swell across the ice pack is consistent with an exponential attenuation on a length scale of 200 km.

1. Introduction

Over the last 30 years, the dramatic reduction in ice cover and thickness in the Arctic is opening larger ocean expanses for wave development [*Thomson and Rogers*, 2014]. Understanding how the waves influence the breaking of ice in floes [e.g., *Williams et al.*, 2013] and how sea ice attenuates surface gravity waves are essential improvements for Earth system models at high latitudes. The representation of sea ice in commonly used numerical wave models is still fairly crude, often based on a partial blocking of wave energy [*Tolman*, 2003]. Wave transformation in sea ice combines a change in phase speed, scattering by ice floes and changes in ice thickness, and dissipation. Recent refinements taking into account both scattering by ice floes and friction below the ice have been introduced by *Doble and Bidlot* [2013]. However, the functional form of parametrizations and the magnitude of the coefficients are still very uncertain due to the paucity of wave measurements in ice-covered waters. Indeed, the usual remote sensing techniques based on altimeter [*Gower*, 1979] and synthetic aperture radar (SAR) [e.g., *Alpers et al.*, 1981] do not allow a measurement of the wave heights in ice-covered waters. At present, only in situ measurements from *Wadhams* [1978] to *Kohout et al.* [2014] are able to document wave attenuation. In spite of intense efforts to augment these data sets, the difficulty of deploying and maintaining instrumentation is the main limitation to our understanding of the interaction of ocean waves with sea ice.

Although ocean waves are clearly visible in SAR imagery of ice-covered oceans, their quantitative analysis is presently limited to the estimation of a dominant wavelength and direction [e.g., *Liu et al.*, 1991; *Shulz-Stellenfleth and Lehner*, 2002]. The radar scattering mechanisms are not fully understood. In the absence of ice, it is well known that the main mechanisms that make it possible to measure waves are the "velocity bunching," explained below, the "tilt" effect which corresponds to a change in backscatter with the surface slope, and the hydrodynamic and aerodynamic modulations that correspond to a change in the amplitude of the scattering features—here waves of a few centimeter wavelengths—along the profile of long waves [*Alpers and Rufenach*, 1981; *Alpers et al.*, 1981; *Vachon et al.*, 2004]. In ice-covered water, the large-scale variation of backscatter with incidence angles is much weaker than in water; hence, the tilting of the icy surface is expected to be negligible. Also, there are no short waves on the surface, and we do not expect a large change in the centimeter-scale geometry of the ice as it heaves up and down with swell. As a result, we expect that the wave patterns come from the velocity bunching effect, which is a misplacement of the scatterers in the direction of motion of the radar antenna (the azimuth). This misplacement is due to the fact that both the position in azimuth and the scatterer velocity toward the radar contribute to the Doppler shift received by the radar. Hence, a homogeneous roughness with a spatial variation of velocities creates

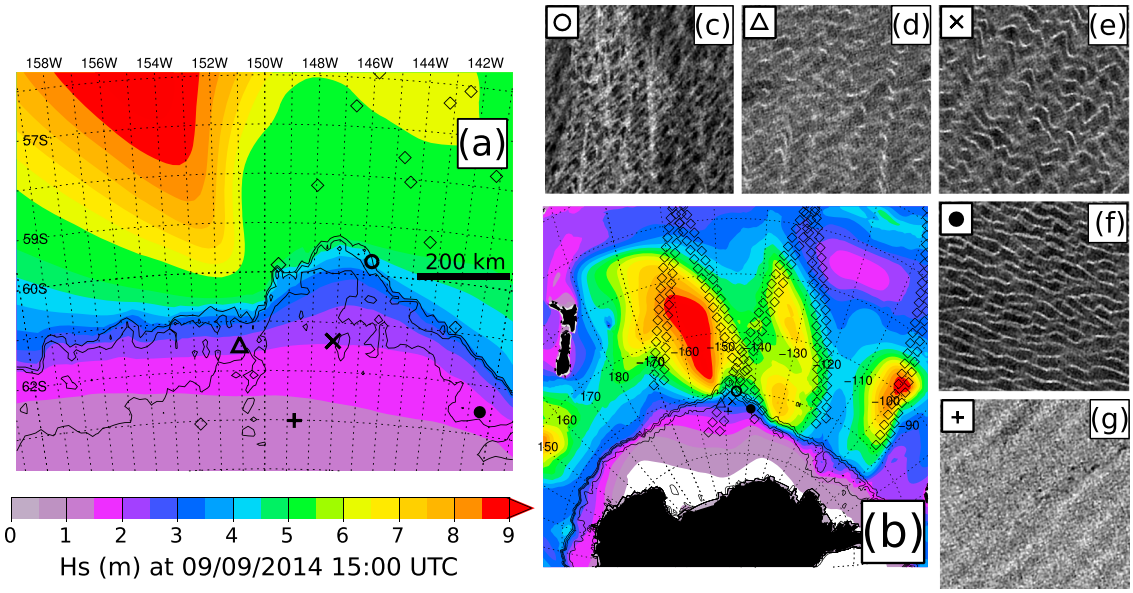

Figure 1. (a) Map for 9 September at 15:00 UTC of the wave heights (colors) predicted by our numerical wave model and sea ice concentration analysis from Special Sensor Microwave Imager (SSM/I) provided by Ifremer/Centre ERS d'Archivage et de Traitement (CERSAT) [*Ezraty et al.*, 2007] based on the Artist Sea Ice (ASI) algorithm by *Kaleschke et al.* [2001]. Contours are drawn at 15%, 30%, and 80%. (b) Regional context of waves and sea ice. The center of wave mode products from Sentinel-1A is indicated by diamonds or other symbols for the particular images analyzed here. (c to g) For those particular images, a 2 by 2 km sample is shown, each is oriented with north up.

patterns in the SAR scene. If the wave orbital velocities are random and strong, this effect produces a blurring in the azimuth direction which makes it impossible to observe the shortest wave components [e.g., *Kerbaol et al.*, 1998]. This is the azimuthal cutoff.

In ice-covered water, the short random waves are absent, so that the waves propagating in azimuth can have the clearest signature. *Lyzenga et al.* [1985] also showed how the velocity bunching transformed straight lines, like the ice edge, into oscillating contours. Here we extend this idea to the analysis of lines within the ice pack. The new SAR instrument on board Sentinel-1A reveals stunning patterns due to its low speckle. Compared to its predecessor Envisat, the speckle is reduced by a factor of 5 and allows new methods for measuring wave heights in ice-covered regions. Further, the use of the acquisition "wave mode" with images spaced along the track every 200 km provides a unique large-scale array of wave measurements, from which wave attenuation can be estimated, extending to the ice-covered ocean the analysis technique of swell dissipation of *Ardhuin et al.* [2009]. We particularly focus on data acquired on 9 September 2014. Section 2 discusses the modulation patterns and the analysis method. Section 3 presents the results for wave heights at different locations and an estimate of wave attenuation. Perspectives follow in section 4.

2. Patterns in SAR Images and Analysis Method

The data used here are Level-1 wave mode products produced experimentally by the Sentinel-1A mission performance center, as part of the calibration and validation phase of the satellite. These are 20 by 20 km square SAR images acquired at the two alternating incidence angles of 23° and 37°, with a resolution of 4 m at the Earth surface, every 200 km along track for each incidence angle. These images can be visualized in the Mission Performance Centre (MPC) Sentinel-1 portal (e.g., http://bit.ly/1xISMxF). Out of the 471 wave mode images acquired on 9 September in the Southern Ocean, we will use data from the ascending track acquired at 04:48:16 UTC and the descending track between 14:26:22 and 14:27:20 UTC, particularly looking at images over sea ice close to the ice edge. The location of these images is shown in Figure 1, and subsets of these images, each 2 by 2 km, is shown in Figures 1c to 1g. The apparent difference in brightness is only due to our adjustment of the grey scale and does not correspond to a change in mean backscatter which varies by less than 10% from one image to another. In this region we expect that the thickness of this seasonal ice is less than 40 cm, based on the IceSAT-derived climatology by *Kurtz and Markus* [2012].

Table 1. Wave Properties in Analyzed Images[a]

	Figure 1c	Figure 1d	Figure 1e	Figure 1f	Figure 1g
Acquisition time (hhmmss)	142622	142706	142651	044816	142720
Incidence angle (deg)	23	37	23	23	23
δ_{rms} (m)	≃80	46	37	20	NA
w_{rms} (m/s)	1.1	0.49	0.39	0.21	NA
$\lambda_{p,2}$ (m)	250	290	250	320	310
$\theta_{p,2}$ (deg)	260	305	306	300	311
$H_{ss,2}$ (m) (method 1)	4.8	3.0	2.1	1.4	NA
$H_{ss,2}$ (m) (method 2)	5–8	3.5	2.2–2.4	1.2	1–1.5
$H_{ss,1}$ (m) (method 2)	1–2	0.8	1.2	1.8	NA
Distance to ice edge (km)	0	60	180	500	200
$\theta_{p,2}$ from model 1 (deg)	285	278	280	260	285
$H_{ss,2}$ from model 1 (m)	4.4	2.4	2.30	0.53	1.3
$H_{ss,1}$ from model 1 (m)	2.2	2.1	0.70	1.34	0.1
$H_{ss,2}$ from model 2 (m)	4.7	3.2	4.1	3.5	3.3
$H_{ss,1}$ from model 2 (m)	2.5	2.1	2.4	2.5	0.8

[a]The ice edge is taken at the 15% sea ice concentration contour, and the distance is counted along the propagation direction of swell 2. The image number correspond to panels in Figure 1. The region of the image analyzed here includes the subimages shown in Figure 1 but with a wider rectangular area, of at least 3 by 3 km, oriented along the azimuth and range. The wavelength and mean direction of swell 2 are $\lambda_{p,2}$ and $\theta_{p,2}$, estimated from the images and our numerical wave model. NA, not applicable.

Within 200 km of the 15% ice concentration contour, all images show a striped pattern with crests oriented from south-west to north-east, with wavelengths ranging from 200 to 500 m, corresponding to wave periods 11 to 18 s according to the linear wave dispersion relation for ice thickness under 50 cm [e.g., *Squire et al.*, 1995]. Most images also contain more closely spaced bright lines oriented east-west with a separation of nearly 150 m. These lines have shapes that range from almost straight, in Figure 1f, to moderately distorted, in Figures 1d and 1e, or completely scrambled in Figure 1c. These lines are also absent in Figure 1g, located further inside the ice. The main purpose of this paper is to provide a quantitative analysis of these patterns, summarized in Table 1, which is validated by a simulation of SAR images.

The two sets of line directions and wavelengths are consistent with orientation and spacing of crests or troughs from two swell systems predicted by our implementation of the WAVEWATCH III model, forced by European Centre for Medium-Range Weather Forecasts winds and sea ice concentrations processed by Ifremer/CERSAT from the SSM/I radiometer. Compared to the description in *Rascle and Ardhuin* [2013], this model implementation uses retuned swell dissipation and whitecapping dissipation, combined with a turbulent generalization of the viscous under-the-ice friction theory in *Liu et al.* [1991] similar to the air-sea friction parametrization in *Rascle and Ardhuin* [2013].

The SAR image and wave modeled spectra for the image partly shown in Figure 1e are shown in Figure 2. The most visible features on the image are the wiggly lines running from west-north-west to east-south-east, corresponding to what we will call "swell 1" coming from 30° with wave number $k = 0.42$ rad/m corresponding to a frequency $f = 0.1$ Hz. This sharp contrast in the SAR images, compared to SAR scenes over water, is made possible by the absence of short wind waves that would otherwise lead to a blurring along the azimuth direction. The spectrum of the SAR image has most of the energy in a range of directions, 300 to 330, and wavelengths 200 to 400 m, that roughly corresponds to the "swell 2" predicted by our wave model. This correspondence is not perfect, and the directions are shifted by 30° counterclockwise in the model (see Table 1). According to the wave model, the most energetic swell is swell 2, coming from the north-west, with heights ranging from 5 to 8 m at the ice edge and a period around 13 s. We expected wave heights of swell 1 to be around 2 m at the ice edge and a peak period of 10 s.

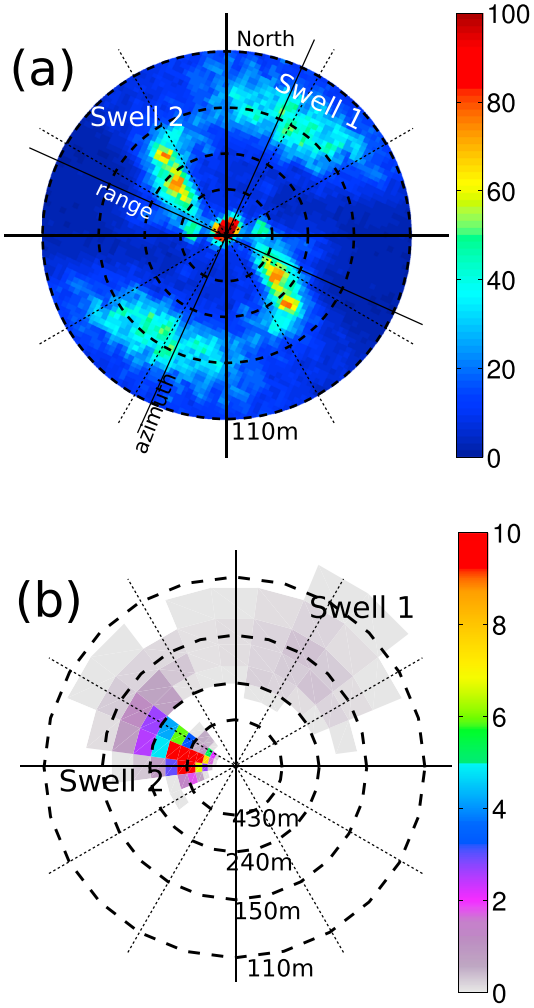

Figure 2. (a) Spectrum of the SAR intensity image corresponding to Figure 1e. (b) Modeled wave spectrum at the same location at 15:00 UTC, with wave directions corresponding to the direction from which the energy is coming. Both observed and modeled spectra contain two main swell systems, a first swell from the north and a second swell from the west. The 180° ambiguity on the direction of wave propagation, when estimated from the intensity of the SAR image alone, is easily removed by using the phase of the cospectrum formed between two image looks using the complex SAR image. Concentric circles correspond to wave frequencies of 0.06, 0.08, 0.1, and 0.12 Hz for linear waves in deep water and in the absence of ice. The color scales are the power spectral density of the normalized SAR image and of the surface elevation directional spectrum.

This difference in direction and the relative magnitude of the two swells compared to the model can be caused by model errors as the effect of ice is poorly represented. In order to effectively interpret the SAR images, we first demonstrate the imaging mechanism and its relationship to the waves. There are no observations of sinuous wave crests in sea ice; hence, this must be an artifact of the SAR processing. We will see below that the SAR processing also produces a shift in the mean direction of the wavy patterns toward the azimuth direction.

We will now quantify the pattern formation in the SAR image. Here we consider that the horizontal orbital velocity is zero due to the ice cover. Given the distance R between Sentinel-1A and sea surface and the relative velocity of the satellite platform V, any vertical velocity w produces a misplacement of a scatterer in the azimuth direction by the distance

$$\delta_A = w \cos\theta_i R/V = wZ/V, \quad (1)$$

where θ_i is the incidence angle and Z is the satellite altitude. With random waves, we get oscillations of this displacement.

For example, a sinusoidal wave of period 10 s and significant wave height 1 m corresponds to a root-mean-square amplitude $a_{rms} = 1/(2\sqrt{2})$ m and orbital velocity $w_{rms} = 1/(2\sqrt{2})2\pi/10 \simeq$ 0.22 m/s. For sentinel-1A the satellite orbit parameters give $Z/V \simeq 94$ s, and the root-mean-square (rms) azimuth misplacement is $\delta_{rms} = 21$ m. The swell number 2, propagating almost along the range direction, introduces a misplacement in azimuth that varies along the range and is thus capable of transforming the straight lines, associated to the convergence lines of swell 1, into curved lines. This mechanism of pattern formation is illustrated in Figure 3 for a small subset of the image already sampled in Figure 1e.

We have also validated this interpretation by a direct simulation of the SAR images. Starting from a surface with a uniform radar cross-section σ_0 at a resolution 10 times finer than the SAR image, we compute the SAR intensity image by averaging, at the SAR resolution, the constant cross section displaced in azimuth as given by equation (1) as a function of the vertical velocity field. A first simulation in one dimension with wave propagating along the azimuth direction gives the results shown in Figures 4a and 4b. It clearly shows, as previously done by *Lyzenga et al.* [1985], that a small wave height can produce a very large contrast: here a 0.5 m swell produces relative intensity changes that exceeds a factor of 3. Also, when the displacement δ_A exceeds the wavelength divided by 2π, the bright regions are doubled, a feature than can be found in Figure 1f. The separation of these twin bright lines grows with increasing velocities, as shown in Figure 4b.

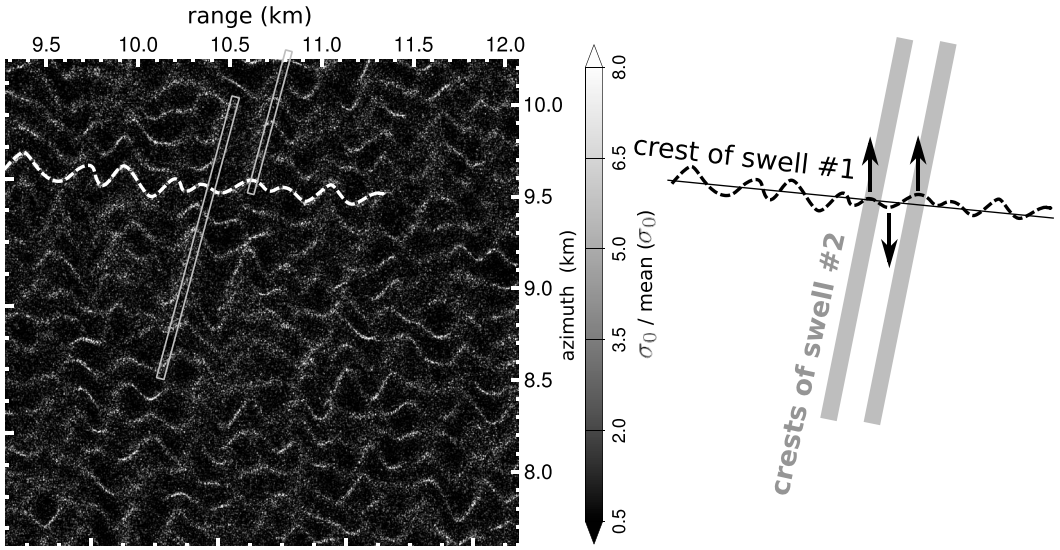

Figure 3. (left) Fragment of a synthetic aperture radar scene acquired by Sentinel-1A in wave mode (HH polarization) on 9 September 2014, at 14:26:54 UTC, around 61.37°S and 147.14°W, in an area where the sea ice coverage estimated from SSM/I exceeds 90%. One of the oscillating bright lines is highlighted with a dashed white line, and the faint thick lines that coincide with deviations of the bright lines is highlighted with two grey rectangles. (right) Interpretation in terms of wave propagation and distortion (arrows) due to the velocity bunching mechanism of the SAR processing which converts velocities in the line of sight in misplacements in the azimuth direction.

In two dimensions, with the range in the x direction and the azimuth in the y direction, these bright regions take linear shapes along contours of $\partial w/\partial y$. Using a realization that combines one or two Gaussian wave packets gives the SAR intensity maps shown in Figures 4d and 4e, with the velocity map combining the two swells shown in Figure 4c. The SAR transformation is strongly anisotropic with a particular signature of gradients in the azimuth direction. This is illustrated by the distortion of the spectrum of wave vertical velocity shown in Figure 4f, which transforms into the image spectrum in Figure 4h. The nonlinear nature of the SAR transformation results in both a broadening of the swell 1 peak and a shift in the direction of the swell 2 peak.

Now that we understand how wave motions create patterns in the SAR images thanks to the SAR model given by equation (1), we can propose different methods to retrieve wave parameters from SAR images. Assuming that the patterns on the image are only a function of the vertical velocity, and not the changes in ice and water properties, it may be possible to invert the field of vertical velocities. Here we first detect linear features from the images and estimate a root-mean-square azimuthal displacement δ_{rms} along them, which provides an estimate of the height of swell number 2. In a second method, we will use direct simulations such as Figures 4d and 4e, to maximize the visual impression of similarity between the SAR image and the simulation.

Starting from the 4 m resolution intensity image, we apply a 3 by 3 pixel smoothing and set a threshold at 1.45 times the average intensity. For each range column (i.e., at a fixed x position) the pixels above the threshold are aggregated, starting from the brighter pixels, by averaging their azimuthal position if they are within 80 m of one another, which is less than the expected swell wavelength. These positions are then tracked from one column to the next. Positions are taken to belong to the same feature if they are within 60 m in azimuth and 60 m in range. An example of tracked features are superimposed on the image in Figure 5. The last step is a supervised decision to accept or reject the features as one single crest or trough. The main difficulty is to avoid tracking errors that can arise from the matching of discontinuous tracks that jump from one feature to another. This semiautomatic tracking of features is impossible for the image shown in Figure 1c, where the oscillation of the features is larger than their separation distance. For that image we have estimated the rms displacement by measuring a few clear

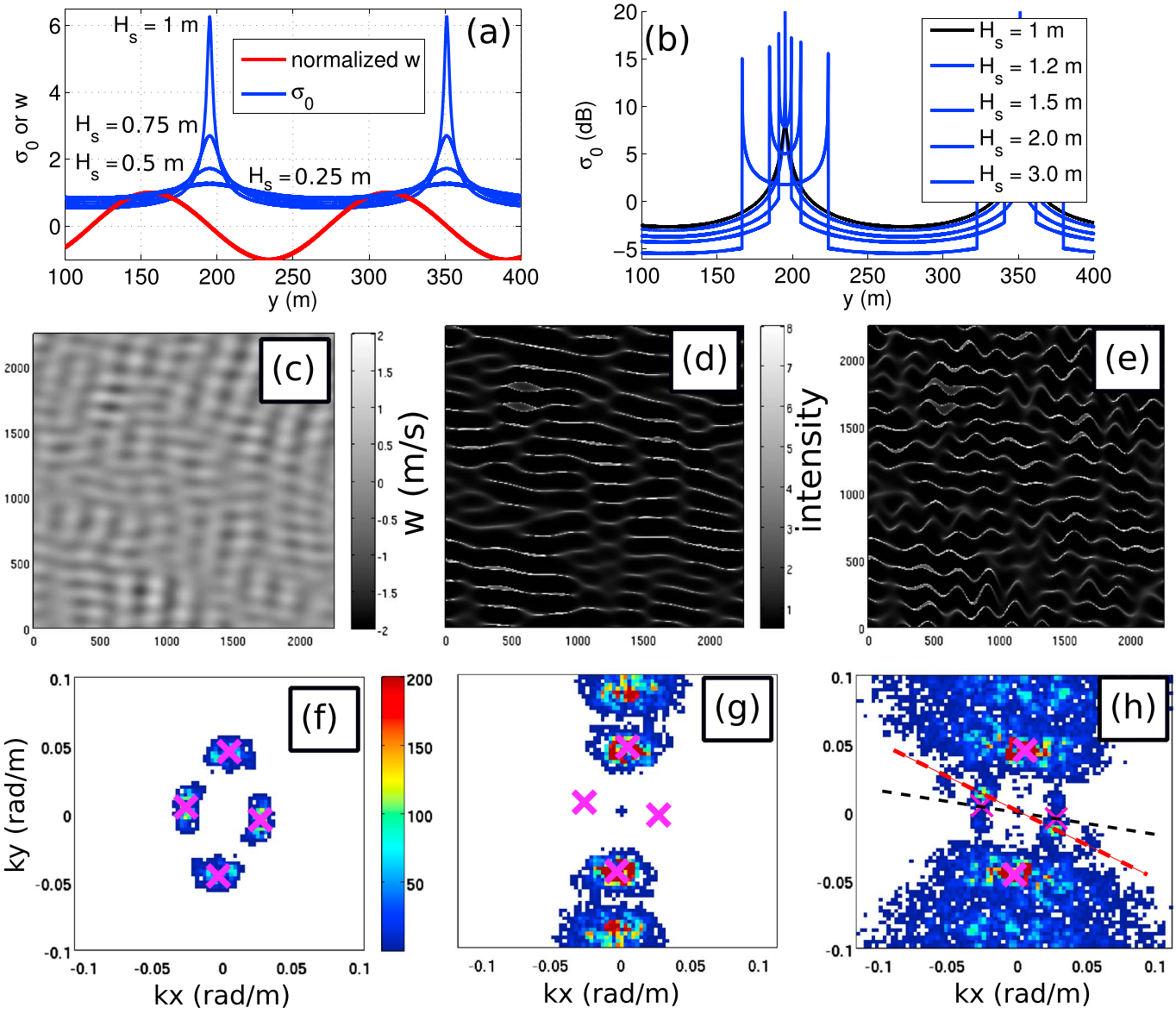

Figure 4. Simulated intensity, normalized by the average intensity. (a) For a monochromatic swell of period $T = 10$ s propagating in the azimuth direction, and amplitudes corresponding to significant wave heights of 0.25, 0.5, 0.75, and 1 m. (b) Same as Figure 4a for larger wave heights, now in log scale. (c) Snapshot of vertical velocity (in m/s), resulting from the superposition of two swell trains with wave height and peak period $H_{s,1} = 1.5$ m, $T_{p,1} = 9.5$ s, $H_{s,2} = 2.4$ m, $T_{p,2} = 12$ s. These swell trains are given by the superposition of 330 independent components with a Gaussian distribution in wave number and in directions. For the first swell these distributions have standard deviations $\sigma_{k,1} = 0.1k_p$, $\sigma_{\theta,1} = 10°$, and $\sigma_{k,1} = 0.12k_p$, $\sigma_{\theta,2} = 15°$. (d) The SAR intensity when only swell 1 is present, and (e) with both swells present. This simulated image shows patterns similar to Figure 1e. The spectra of Figures 4c–4e are shown in Figures 4f–4h, respectively, and pink crosses show the spectral location of the two swell peaks. The direction of the image peak in Figure 4h, shown with the dashed red line, is shifted 18° toward the azimuth direction compared to the true swell direction, shown with the black dashed line.

oscillations. Based on the analysis above, we expect the significant height of the second swell, H_{ss2}, to be given by

$$H_{ss2} = 2\sqrt{2}\frac{\delta_{\text{rms}} V}{Z\sqrt{2\pi g/\lambda_{p,2}}}, \tag{2}$$

and $\lambda_{p,2}$ is the peak wavelength from which we estimate the peak radian frequency using the linear dispersion relation without ice, $\sigma_{p,2} = \sqrt{2\pi g/\lambda_{p,2}}$. This expression does not depend on the direction of propagation of the swell because we have assumed that the horizontal velocities of the ice layer are zero,

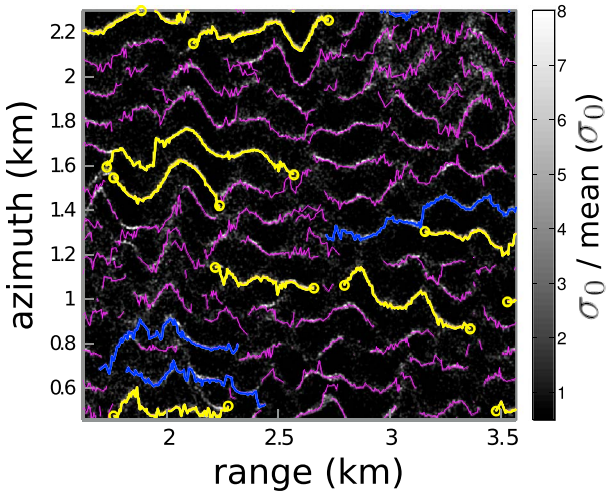

Figure 5. Fragment of the image illustrated by Figure 1e, with a smoothing applied and the feature detection algorithm. All detected features are in magenta. The 30 longest segments are colored differently: in blue if they have not been accepted as one continuous crest, and in yellow if they have been accepted. For the lines in yellow here, the value of δ_{rms} is 32 m.

which would be the case for a continuous elastic layer of ice. For ice broken into floes, which is probably the case in most images analyzed here, there should be a horizontal velocity too. Multiplied by the cosine of the incidence angle and the cosine of the wave propagation relative to the range, this horizontal velocity would contribute to the measured Doppler shifts. For the sake of simplicity we do not consider this horizontal component.

Our feature tracking algorithm works best for low noise levels and straight lines, which are easier to track, leading to a possible underestimation of δ_{rms} when it is large. Noise and short crestedness can, on the contrary, lead to a positive bias when δ_{rms} is low. Results are also affected by the choice of the intensity threshold and the distance tolerances for tracking the features.

To evaluate these effects, we have tested a second method, based on the direct simulation of the SAR scene assuming a uniform surface roughness without taking into account thermal and speckle noises. As an example, the image acquired at 14:27:06 UTC and illustrated in Figures 2 and 4 gives a $\delta_{rms} \simeq 37$ m with the first method, leading to $H_{ss2} = 2.1$ m. When this value is used to simulate SAR images, the lines appear more straight than in the SAR image, which confirms the expected underestimation by the first method. The direct simulation also provides some access to the height of the first swell via the distribution of intensities and the presence or absence of doubled features as in Figures 4b and 1f, which occur for $H_s > 1.5$ m in the case of a 10 s wave in the azimuth direction.

3. Wave Heights and Attenuation in the Regional Context

Wave parameters for the second swell were estimated from the images for which the crest wiggles can be measured (Figures 1c–1f), and also Figure 1g using our second method, with values given in Table 1. In order to evaluate their consistency, these SAR-derived values are compared to two numerical model estimates. In model 1, a dissipation parametrization is included based on friction below the ice and a constant under-ice roughness of 1 mm. In model 2, no dissipation at all is included.

Although the wave field is not stationary, the strong gradient in wave height near the ice edge is clearly due to the interaction of waves and ice and happens at a scale much shorter than the effects of dispersion and dissipation in the absence of ice, both documented by *Ardhuin et al.* [2009]. From the data alone we can estimate an *e*-folding scale for the wave energy that is of the order of 200 km, and generally consistent with measurements for such long swells reported by *Doble and Bidlot* [2013] or *Kohout et al.* [2014]. Using a numerical model in combination with this kind of estimate can also help correct for propagation effects, in particular taking into account the fact that the ice edge is not straight and the wave field varies in the two horizontal dimensions. A routine analysis of SAR imagery with a similar resolution and large coverage should help build up a very useful database for documenting the attenuation of waves in the marginal ice zone.

The use of simulations of SAR scenes in our second method could also be used to estimate the attenuation of swell 1. In particular, our simulations show that the height of swell 1 should be less than 0.2 m in Figure 1g; otherwise, bright lines should be visible.

4. Summary and Perspectives

Lyzenga et al. [1985] had already observed that in ice-covered conditions, the distortion of SAR images by swell orbital velocities, known as the velocity bunching, is generally constructive and yields a wavy pattern. This is because the short waves, which lead to a destructive effect in open water, have been damped by the ice cover. Here we have analyzed very clear wave patterns in the presence of two swell trains propagating at different angles. The velocity bunching of the swell propagating along the azimuth direction produces a pattern of bright lines and just like sunlight creates bright lines at the bottom of a shallow swimming pool. The analogy is that the intensity in the SAR image is focused by variations of vertical velocity in the azimuth direction, whereas light at the bottom of a pool is focused by refraction at the wavy air-water interface. In the SAR image, a second swell that propagates closer to the range direction causes a meandering of these lines. The size of these meanders in the azimuth direction is proportional to the vertical velocity at the sea surface. Combined with an estimation of the wavelength of the second swell and using the wave dispersion relation, we have inferred significant heights of the second swell, without any assumption on the modulation transfer function, which are usually used for ice-free surfaces.

This nonlinear imaging caused by the velocity bunching of the combination of two swells in the SAR image is a clear example of a strong limitation of the quasi-linear assumption which is used in some algorithms for ice-free waters [*Chapron et al.*, 2001; *Collard et al.*, 2005]. That assumption is expected to fail for large swell orbital velocities in the azimuth direction [e.g., *Collard et al.*, 2009]. The SAR images analyzed here also show that the directional spreading of the first swell contains information about the crest meandering caused by the second swell, which should not be confused with a short crestedness of the first swell. Also, our simulations show that the mean direction can be biased away from the range direction. Hence, the interpretation of mean direction and directional spreading in spectra of SAR intensity images should be taken with caution and cannot be attributed completely to a real directional spreading caused by processes such as wave scattering by ice floes [e.g., *Wadhams et al.*, 1986].

The wave mode in Sentinel-1A data is a unique source of sparse high-resolution measurements of the roughness of the ocean surface that made the present study possible. To our knowledge, there is unfortunately not yet a plan to disseminate the corresponding level 1 data to the scientific community. We hope to have demonstrated the possible uses of these data in ice-covered regions, and we also expect other applications in different ocean conditions. In general, the level 1 data can be a unique source of high-resolution roughness that sample the strong variability of the oceanic and atmospheric features, which will help in the design of future high-resolution sensors. The wave patterns shown here were also found in Interferometric Wide swath mode data that have been acquired by Sentinel-1A in the Arctic since January 2015.

Acknowledgments

F.A., F.G.-A., F.C., and G.G. are supported by EU-FP7 project SWARP under grant agreement 607476, with additional support from Labex Mer via grant ANR-10-LABX-19-01. L1 data have been processed by ESA PDGS and circulated to the Sentinel-1 A Misssion Performance Center for Sentinel-1 A cal/val activities in the framework of ESA contract "Preparation and Operations of the Mission Performance Centre (MPC) for the GMES SENTINEL-1 Mission" (4000107360/12/I-LG). Comments by anonymous reviewers and the Editor led to a much improved version of this paper.

The Editor thanks two anonymous reviewers for their assistance in evaluating this paper.

References

Alpers, W. R., and C. L. Rufenach (1981), The effect of orbital motions on synthetic aperture radar imagery of ocean waves, *IEEE Trans. Antennas Propag.*, *27*(C7), 685–690.

Alpers, W. R., D. B. Ross, and C. L. Rufenach (1981), On the detectability of ocean surface waves by real and synthetic aperture radar, *J. Geophys. Res.*, *86*(C7), 6481–6498.

Ardhuin, F., B. Chapron, and F. Collard (2009), Observation of swell dissipation across oceans, *Geophys. Res. Lett.*, *36*, L06607, doi:10.1029/2008GL037030.

Chapron, B., H. Johnsen, and R. Garello (2001), Wave and wind retrieval from SAR images of the ocean, *Ann. Telecommun.*, *56*, 682–699.

Collard, F., F. Ardhuin, and B. Chapron (2005), Extraction of coastal ocean wave fields from SAR images, *IEEE J. Oceanic Eng.*, *30*(3), 526–533.

Collard, F., F. Ardhuin, and B. Chapron (2009), Monitoring and analysis of ocean swell fields using a spaceborne SAR: A new method for routine observations, *J. Geophys. Res.*, *114*, C07023, doi:10.1029/2008JC005215.

Doble, M. J., and J.-R. Bidlot (2013), Wave buoy measurements at the Antarctic sea ice edge compared with an enhanced ECMWF WAM: Progress towards global waves-in-ice modelling, *Ocean Model.*, *70*, 166–173, doi:10.1016/j.ocemod.2013.05.012.

Ezraty, R., F. Girard-Ardhuin, J. F. Piollé, L. Kaleschke, and G. Heygster (2007), Arctic and Antarctic sea ice concentration and Arctic sea ice drift estimated from special sensor microwave imager data. User's manual, version 2.1, *Tech. Rep.*, Ifremer/CERSAT, Brest, France.

Gower, J. F. R. (1979), The computation of ocean wave heights from GEOS-3 satellite radar altimeter, *Remote Sens. Environ.*, *8*, 97–114.

Kaleschke, L., C. Lüpkes, T. Vihma, J. Haarpaintner, A. B. J. Hartmann, and G. Heygster (2001), SSM/I sea ice remote sensing for mesoscale ocean-atmospheres, *Can. J. Remote Sens.*, *27*(5), 526–537.

Kerbaol, V., B. Chapron, and P. Vachon (1998), Analysis of ERS-1/2 synthetic aperture radar wave mode imagettes, *J. Geophys. Res.*, *103*(C4), 7833–7846.

Kohout, A. L., M. J. M. Williams, S. M. Dean, and M. H. Meylan (2014), Storm-induced sea-ice breakup and the implications for ice extent, *Nature*, *509*, 604–607, doi:10.1038/nature13262.

Kurtz, N., and T. Markus (2012), Satellite observations of Antarctic sea ice thickness and volume, *J. Geophys. Res.*, *117*, C08025, doi:10.1029/2012JC008141.

Liu, A. K., B. Holt, and P. W. Vachon (1991), Wave propagation in the marginal ice zone' model predictions and comparisons with buoy and synthetic aperture radar data, *J. Geophys. Res.*, *96*(C3), 4605–4621.

Lyzenga, D. R., R. A. Shuchman, J. D. Lyden, and C. L. Rufenach (1985), SAR imaging of waves in water and ice: Evidence for velocity bunching, *J. Geophys. Res.*, *90*, 1031–1036.

Rascle, N., and F. Ardhuin (2013), A global wave parameter database for geophysical applications. Part 2: Model validation with improved source term parameterization, *Ocean Model.*, *70*, 174–188, doi:10.1016/j.ocemod.2012.12.001.

Shulz-Stellenfleth, J., and S. Lehner (2002), Spaceborne synthetic aperture radar observations of ocean waves traveling into sea ice, *J. Geophys. Res.*, *107*(C8), 3106, doi:10.1029/2001JC000837.

Squire, V., J. Dugan, P. Wadhams, P. Rottier, and A. Liu (1995), Of ocean waves and sea ice, *Annu. Rev. Fluid Mech.*, *27*(3), 115–168.

Thomson, J., and W. E. Rogers (2014), Swell and sea in the emerging Arctic Ocean, *Geophys. Res. Lett.*, *509*, 3136–3140, doi:10.1002/2014GL059983.

Tolman, H. L. (2003), Treatment of unresolved islands and ice in wind wave models, *Ocean Model.*, *5*, 219–231.

Vachon, P. W., F. M. Monaldo, B. Holt, and S. Lehner (2004), Chapter 5. Ocean surface wave spectra, in *Synthetic Aperture Radar Marine User's Manual, Oceanology*, vol. 6, edited by C. R. Jackson and J. R. Apel, pp. 139–169, U.S. Dep. of Commer., NOAA/NESDIS/ORA, Washington, D. C.

Wadhams, P. (1978), Attenuation of swell by sea ice, *J. Geophys. Res.*, *78*, 3552–3563.

Wadhams, P., V. A. Squire, J. A. Ewing, and R. W. Pascal (1986), The effect of the marginal ice zone on the directional wave spectrum of the ocean, *J. Phys. Oceanogr.*, *16*, 358–376.

Williams, T. D., L. G. Bennetts, V. A. Squire, D. Dumont, and L. Bertino (2013), Wave-ice interactions in the marginal ice zone. Part 1: Theoretical foundations, *Ocean Model.*, *70*, 81–91, doi:10.1016/j.ocemod.2013.05.010.